Astronomy
&
Astrophysics

Suzaku study of gas properties along filaments of A2744

Y. Ibaraki[1], N. Ota[1], H. Akamatsu[2], Y.-Y. Zhang[3], and A. Finoguenov[4]

[1] Department of Physics, Nara Women's University, Kitauoyanishimachi, Nara, 630-8506 Nara, Japan
   e-mail: `naomi@cc.nara-wu.ac.jp`
[2] SRON Netherlands Institute for Space Research, Sorbonnelaan 2, 3584 CA Utrecht, The Netherlands
[3] Argelander Institute for Astronomy, Bonn University, Auf dem Hügel 71, 53121 Bonn, Germany
[4] Department of Physics, University of Helsinki, Gustaf Hällströmin katu 2a, 00014 Helsinki, Finland

ABSTRACT

Context. We present the results of *Suzaku* observations of a massive galaxy cluster A2744, which is an active merger at $z = 0.308$.
Aims. By using long X-ray observations of A2744, we aim to understand the growth of the cluster and the gas heating process through mass accretion along the surrounding filaments.
Methods. We analyzed data from two-pointed *Suzaku* observations of A2744 to derive the temperature distribution out to the virial radius in three different directions. We also performed a deprojection analysis to study radial profiles of gas temperature, density, and entropy and compared the X-ray results with multiwavelength data to investigate correlations with the surface density of galaxies and with radio relics.
Results. The gas temperature was measured out to the virial radius r_{200} in the north-eastern region and to about $1.5r_{200}$ in the north-western and southern regions. The radial profile of the gas temperature is rather flat and the temperature is very high (even near r_{200}), which makes it comparable to the mean temperature of this cluster ($kT = 9$ keV). These characteristics have not been reported in any other cluster. We find a hint of temperature jump in the north-eastern region whose location coincides with a large radio relic, indicating that the cluster experienced gas heating because of merger or mass accretion onto the main cluster. The temperature distribution is anisotropic and shows no clear positive correlation with the galaxy density, which suggests an inhomogeneous mass structure and a complex merger history in A2744.

Key words. galaxies: clusters: individual: A2744 – galaxies: clusters: intracluster medium – X-rays: galaxies: clusters – cosmology: observations

1. Introduction

A2744 at $z = 0.308$ (AC118 or RXC J0014.3–3022) is one of the most actively merging clusters, and it is nicknamed "Pandora's cluster" (e.g., Owers et al. 2011). This cluster is also known as a gravitational lens with an enormous mass ($M = 1.8 \times 10^{15}\ M_\odot$ for $r < 1.3$ Mpc; Merten et al. 2011). Braglia et al. (2007) discovered two large-scale filamentary structures that extend beyond the virial radius of A2744. Given this well-defined large-scale structure, A2744 offers a unique opportunity to study the formation and growth of a massive cluster in the distant universe through merging and mass accretion along the filaments.

The mass structure and characteristics of the intracluster medium (ICM) in the core of A2744 have been extensively studied at various wavelengths. In the X-ray region, the cluster exhibits two emission peaks that correspond to the main cluster and to a subcluster in the northwest. A bow shock was discovered in the subcluster by *Chandra* (Kempner & David 2004). Consistent with this discovery, in the central region of the system, two overdensities of member galaxies appear that are clearly separated from the two X-ray subcomponents visible in the *XMM-Newton* image (e.g., Pierini et al. 2008; Zhang et al. 2004, 2006; Finoguenov et al. 2005). Merten et al. (2011) performed a detailed lensing and X-ray analysis that suggests that the southern and northwestern cores are post-merger and that they exhibit a morphology similar to that of the Bullet Cluster viewed from a different angle.

The radio halo in A2744 is one of the most luminous, and the bulk of the diffuse radio emission is centered on the main cluster. The cluster also hosts a large radio relic at a projected distance of 2 Mpc (Govoni et al. 2001a,b). This suggests that shock heating is at work; however, owing to the lack of deep X-ray data, the detailed characteristics of the ICM at the location of relic have yet to be clarified. Furthermore, within $r = 1$ Mpc, the dynamical mass is calculated to be $(1.4–2.4) \times 10^{15}\ M_\odot$ (Boschin et al. 2006). This value is greater than the X-ray hydrostatic mass by ~40%, and it is likely to be overestimated because of mergers. Thus, A2744 calls for an assessment of the characteristics of its complex ICM beyond the virial radius.

The X-ray Imaging Spectrometer (XIS; Koyama et al. 2007) onboard the *Suzaku* satellite (Mitsuda et al. 2007) enabled observations of diffuse ICM emission up to their virial radius because of the low and stable background. Thus far, XIS has measured temperature profiles in the cluster outskirts for about twenty nearby objects, all of which show a temperature drop by a factor of two to four at large radii (for a review, see Reiprich et al. 2013). Recently, Ichikawa et al. (2013) have reported a similar temperature decrease in a cool-core cluster A1835 at $z = 0.25$. Beyond that redshift, we still lack data. Theoretically, the mass accretion and formation shock may tend to occur at high redshifts. Thus, a detailed study of the outer regions of distant mergers is important for probing the formation history of clusters.

With the goal of understanding cluster growth via mass accretion and gas heating, we focus on A2744 and measure the
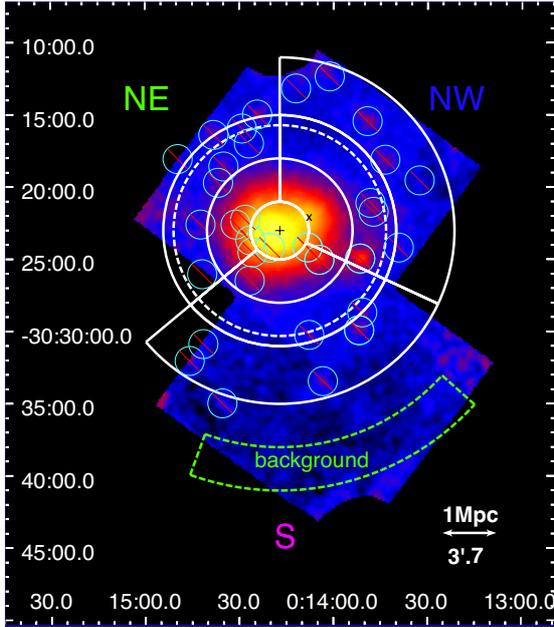
Fig. 1. *Suzaku* XIS-0 + XIS-1 + XIS-3 mosaic image of A2744 in the 0.5–8 keV band. The image is corrected for exposure map and vignetting effects and is smoothed by a Gaussian function with $\sigma = 24''$. No background was subtracted. The X-ray peaks of the main cluster and the NW subcluster are marked with "+" and "x", respectively. The spectral integration regions ($0'-2', 2'-5', 5'-8', 8'-12'$) are shown with the white annuli, while point sources detected by *XMM-Newton* PN and MOS are eliminated with an $r = 1'$ radius (the cyan circles with red diagonal lines). The dashed white line denotes the virial radius $r_{200} = 7'.3$. A fan-shaped $r = 15'-18'$ region in the south (green) was used to estimate background. The two corners of the CCD chip illuminated by ^{55}Fe calibration sources are excluded from the image.

large-scale temperature distribution with *Suzaku*. This paper is organized as follows. In Sect. 2 the *Suzaku* observations and data reduction are presented, in Sect. 3 the spectral analysis and results are shown, in Sect. 4 the temperature profile of A2744 is compared with other clusters, and the ICM characteristics are discussed based on a comparison with the galaxy density in the filaments and the radio relic. In Sect. 5 we summarize the results.

Throughout the paper, the cosmological model is adopted with matter density $\Omega_M = 0.27$, cosmological constant $\Omega_\Lambda = 0.73$, and Hubble constant $H_0 = 70$ km s^{-1} Mpc^{-1}. At the cluster redshift ($z = 0.308$), $1'$ corresponds to 274 kpc. Unless otherwise noted, the specified errors indicate a 90% confidence interval.

2. Observation and data reduction

The present study uses *Suzaku* XIS data of A2744 taken during two pointed observations, one centered on the main cluster and the other on the S region. The net exposure times were 150 ks and 67 ks for the center and the S regions, respectively. The summary of the observation log is given in Table 1. The XIS detectors consist of four X-ray-sensitive CCD cameras, three front-illuminated CCDs (XIS-0, XIS-2, XIS-3), and one back-illuminated CCD (XIS-1) (Koyama et al. 2007). Among them, XIS-0, XIS-1, and XIS-3 were operated in normal modes during the observations and the space charge injection option was applied (Uchiyama et al. 2008).

Figure 1 shows the XIS mosaic image of A2744 in the 0.5−8 keV energy band. Thus, the XIS field of view covers the ICM emission out to the cluster virial radius $r_{200} = 2.0$ Mpc (see

Sect. 3.1) and beyond. As seen in Fig. 1, the X-ray morphology is irregular, with elongation along the W-E direction and bimodal X-ray-emission peaks at the center.

We used cleaned event files created by the pipeline processing version 2.4 and performed the data analysis using HEASoft ver 6.12 and CALDB version 2012-09-02 for XIS and version 2011-06-30 for the X-ray telescopes (XRT; Serlemitsos et al. 2007). The XIS data were filtered according to the following criteria: Earth elevation angle >10°, day-Earth elevation angle >20°, and the satellite outside the South Atlantic Anomaly.

To measure the average ICM temperature, the X-ray spectra were extracted from the full XIS field of view in the central pointing. Throughout the spectral analysis, point sources detected by *XMM-Newton* were removed with an $r = 1'$ circle. To investigate the radial distributions, we analyzed the spectra integrated from annular regions centered on the X-ray centroid, (RA, Dec) = (00:14:17.1, −30:23:02.6) (Ota & Mitsuda 2004). The radial ranges of the spectra were $0'-2', 2'-5', 5'-8'$, and $8'-12'$, and they were divided into the three azimuthal directions NW, NE, and S (Fig. 1) because two filaments were identified in the NW and S directions (Braglia et al. 2007). The spectra were rebinned so that each spectral bin contained more than 60 counts for spectra in the center and 80 counts for spectra in the S.

The non-X-ray background was subtracted using `xisnxbgen` (Tawa et al. 2008). The other background components, i.e., the cosmic X-ray background (CXB) and the Galactic X-ray emission arising from the Local Hot Bubble (LHB) and the Milky Way Halo (MWH), were assessed by using the same model as used in Sakuma et al. (2011) and in Ota et al. (2013). The background spectra in the S ($15' < r < 18'$) were fit to the model "apec$_{LHB}$+phabs(apec$_{MWH}$+power-law$_{CXB}$)", which yielded the parameters given in Table 2, where the spectral normalization factors were derived assuming that these X-ray background components have uniform surface brightness distributions within $r = 20'$ centered on the XIS optical axis. According to this model, the X-ray background in each spectral region was simulated by using the XSPEC fakeit command and then subtracted from the observed spectrum.

We used `xisrmfgen` to generate the energy response file. To consider the XRT's vignetting effect and a decrease in the low-energy efficiency because of the contaminating material on the optical blocking filter of the XIS, the auxiliary response files were calculated by using `xissimarfgen` (Ishisaki et al. 2007). For input cluster surface brightness, we assumed a β-model image with $\beta = 0.96$ and $r_c = 2'.2$ (Ota & Mitsuda 2004).

3. Analysis and results

3.1. Global spectra in center

To measure the average temperature of A2744, we first analyzed the XIS spectra extracted from an $18' \times 18'$ square in the central pointing (Fig. 1). The observed 0.5–8 keV spectra of three sensors (XIS-0, XIS-1, and XIS-3) were simultaneously fit to the APEC thermal plasma model (Smith et al. 2001) (Fig. 2). The cluster redshift and Galactic hydrogen column density were fixed at $z = 0.308$ and $N_H = 1.39 \times 10^{20}$ cm^{-2} (LAB survey; Kalberla et al. 2005), respectively. For metal abundance, we used the tables in Anders & Grevesse (1989). The χ^2 fitting was performed using XSPEC version 12.7.1

The model parameters are given in Table 3. The resulting global temperature and metal abundance are $kT = 9.0 \pm 0.2$ keV and $Z = 0.21 \pm 0.02$ solar, respectively, which agree well with the previous ASCA measurement (Ota & Mitsuda 2004).

Table 1. *Suzaku* observation log.

Object	OBSID	Date	RA[a]	Dec[a]	Exposure (s)[b]
A2744 Center	802033010	2007 Jul. 19–23	00:14:9.5	−30:20:40.6	150 583
A2744 South	805015010	2010 Dec. 10–12	00:14:3.2	−30:33:2.9	67 428

Notes. [a] Pointing coordinates in J2000. [b] Net exposure time after data filtering.

Table 2. Spectral fits to background data for CXB and Galactic components.

Γ	Norm[a] ($\times 10^{-4}$)	kT_{MWH} [keV]	$Norm_{MWH}$[b] ($\times 10^{-3}$)	kT_{LHB} [keV]	$Norm_{LHB}$[b] ($\times 10^{-2}$)	χ^2/d.o.f.
1.40(fixed)	$5.83^{+0.38}_{-0.46}$	$0.34^{+0.24}_{-0.34}$	$0.38^{+2.34}_{-0.38}$	$0.13^{+0.47}_{-0.13}$	$0.14^{+1.07}_{-0.14}$	38.7/38

Notes. [a] Photon flux of power-law model, in units of photons keV^{-1} cm^{-2} s^{-1} at 1 keV. [b] Normalization of the APEC model, norm $= \int n_e n_H dV/(4\pi(1+z)^2 D_A^2)$ [10^{-14}cm^{-5}]. D_A is the angular diameter distance to the source. An $r = 20'$ uniform sky is assumed.
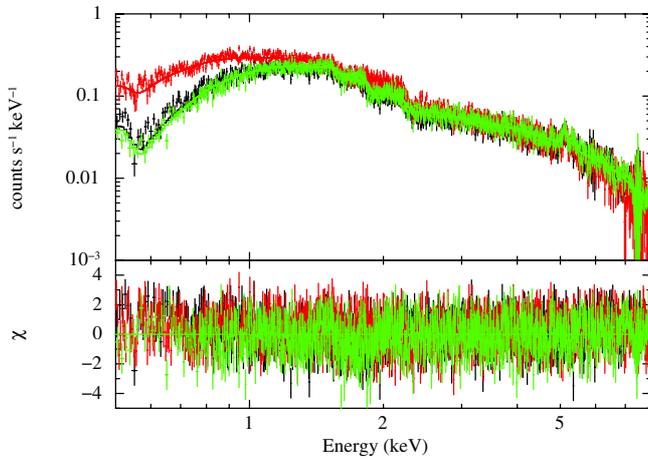

Fig. 2. XIS spectra of A2744 center. XIS-0 (black), XIS-1 (red), XIS-3 (green) are shown separately. The solid lines in the *upper panel* show the best-fit APEC model convolved with the telescope and detector response functions.

Fig. 3. Example of analysis of annular spectra of Sect. 3.2. Fit to XIS spectra in NE $5'-8'$ region is based on APEC model.

Table 3. APEC model parameters for spectra of A2744 center.

kT [keV]	Z [solar]	Norm	χ^2/d.o.f.
$9.00^{+0.20}_{-0.20}$	$0.21^{+0.02}_{-0.02}$	$9.91^{+0.08}_{-0.08} \times 10^{-3}$	2993/2739

Substituting a mean temperature of $kT = 9.0$ keV into the $R-T$ relationship (Arnaud et al. 2005) gives a virial radius of $r_{200} = 2.0$ Mpc or $7'.3$.

3.2. Annular spectra in three directions

To derive the radial temperature profiles along the filaments, we extracted spectra from the concentric rings: $0'-2'$, $2'-5'$, $5'-8'$, and $8'-12'$, as shown in Fig. 1. The azimuthal angles in three directions are NW: $335°-90°$, NE: $90°-220°$, and S: $220°-335°$, respectively, and All: $0°-360°$ is used for the azimuthally averaged profile. For the NE direction, $8'-12'$ is outside the XIS field of view. No significant cluster emission is detected beyond $12'$ from the cluster center in the S direction, which was not used in the present analysis.

XIS-0, XIS-1, and XIS-3 spectra in each ring were then simultaneously fit to the APEC model in the same manner as
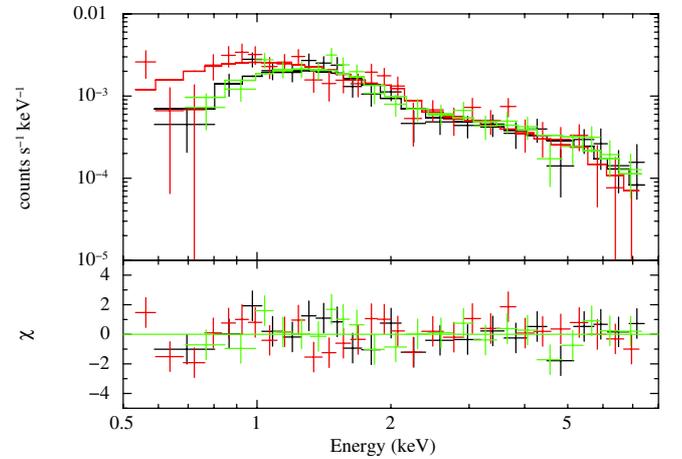
mentioned above. Figure 3 shows an example of spectral fitting for the case of the NE region. The best-fit parameters are listed in Table 4, and the projected temperature profiles are plotted in Fig. 4.

We successfully obtained the radial temperature profile up to r_{200} for NE and $1.5 r_{200}$ for NW and S for the first time. The temperature near the virial radius is associated with relatively large statistical uncertainty; however, the result suggests that the profile is rather flat. The temperature outside r_{200} is comparable to the global temperature (~9 keV) and does not decline significantly, as is often seen in other clusters.

Furthermore, the temperature distribution is anisotropic as there is also a hint of temperature jump near r_{200} in the NE, while the temperature is lowest in the S direction at the same radius, which is discussed in more detail later.

3.3. Systematic errors in temperature measurement

To check the robustness of the temperature measurement in the cluster outskirts, we consider possible systematic errors due to (i) the background model; and (ii) the effect of the XRT's point spread function (PSF), and we examine; (iii) possible contamination of the cluster spectra from point sources in the NE region.

– For (i), we found that the 2−10 keV CXB flux estimated from A2744 south is 30% lower than that of a blank-sky spectrum

Table 4. APEC model parameters obtained from analysis of annular spectra from A2744.

			All	
Region	$0'-2'$[a]	$2'-5'$	$5'-8'$	$8'-12'$
kT [keV]	$10.20^{+0.31}_{-0.31}$	$8.69^{+0.36}_{-0.32}$	$8.16^{+1.05}_{-0.84}$	–
Z [solar]	$0.24^{+0.04}_{-0.04}$	$0.19^{+0.04}_{-0.04}$	$0.24^{+0.13}_{-0.12}$	–
Norm	$5.49^{+0.81}_{-0.81} \times 10^{-3}$	$4.66^{+0.07}_{-0.08} \times 10^{-3}$	$1.24^{+0.06}_{-0.06} \times 10^{-3}$	–
χ^2/d.o.f.	1032/956	841/750	323/289	–
			NW	
Region	$0'-2'$	$2'-5'$	$5'-8'$	$8'-12'$
kT [keV]	–	$8.09^{+0.31}_{-0.31}$	$8.05^{+1.47}_{-1.12}$	$9.92^{+3.90}_{-2.24}$
Z [solar]	–	$0.23^{+0.05}_{-0.05}$	$0.17^{+0.16}_{-0.16}$	$0.38^{+0.43}_{-0.38}$
Norm	–	$5.13^{+0.11}_{-0.11} \times 10^{-3}$	$1.26^{+0.09}_{-0.08} \times 10^{-3}$	$1.05^{+0.13}_{-0.12} \times 10^{-3}$
χ^2/d.o.f.	–	570/546	246/197	221/189
			NE	
Region	$0'-2'$	$2'-5'$	$5'-8'$	$8'-12'$
kT [keV]	–	$9.35^{+0.74}_{-0.73}$	$13.58^{+8.17}_{-4.41}$	–
Z [solar]	–	$0.21^{+0.08}_{-0.08}$	$0.29^{+0.75}_{-0.29}$	–
Norm	–	$3.98^{+0.13}_{-0.13} \times 10^{-3}$	$1.11^{+0.15}_{-0.16} \times 10^{-3}$	–
χ^2/d.o.f.	–	283/294	60.6/73	–
			S	
Region	$0'-2'$	$2'-5'$	$5'-8'$	$8'-12'$
kT [keV]	–	$8.98^{+0.90}_{-0.85}$	$5.56^{+1.00}_{-0.77}$	$6.99^{+5.97}_{-2.16}$
Z [solar]	–	$0.06^{+0.09}_{-0.06}$	$0.25^{+0.23}_{-0.21}$	$0.61^{+0.90}_{-0.61}$
Norm	–	$4.56^{+0.17}_{-0.16} \times 10^{-3}$	$1.32^{+0.13}_{-0.13} \times 10^{-3}$	$0.63^{+0.17}_{-0.16} \times 10^{-3}$
χ^2/d.o.f.	–	271/236	170/145	45.3/62

Notes. [a] The innermost region is a circle with $r = 2'$, which is common to the three directions.
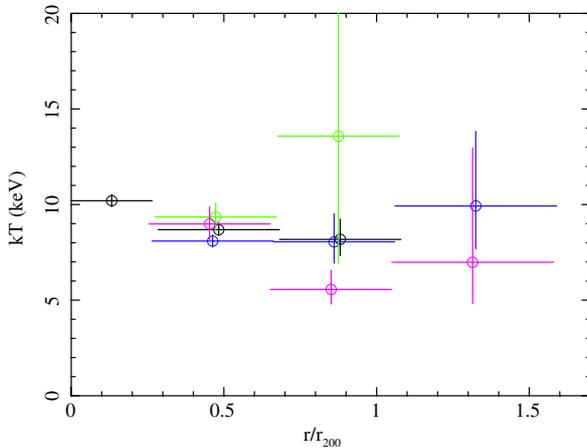

Fig. 4. Projected temperature profiles obtained from XIS spectral analysis: All (black), NW (blue), NE (green), S (magenta).

from the XIS data of the Lockman Hole and 36% lower than what is obtained with the ASCA Medium Sensitive Survey and Large Sky Survey (Kushino et al. 2002). We confirmed this trend by comparing the ROSAT PSPC spectra of annular regions around A2744 and around the Lockman Hole, which we retrieved from the ROSAT All-Sky Survey diffuse background map (Snowden et al. 1997). Considering the typical large-scale fluctuations of $1\sigma \sim 7\%$ (Kushino et al. 2002), the probability that we would observe this low intensity is likely to be low; however, we use the present CXB model in Table 2 as the nominal case for A2744 and examine the impact of background uncertainty in a more quantitative manner below.

The statistical fluctuation of the source number count in the XIS field of view gives the CXB brightness fluctuation expressed as $\sigma_{CXB}/I_{CXB} \propto \Omega_{Bgd}^{-0.5} S_c^{0.25}$. Here Ω_{Bgd} is the effective solid angle and S_c the energy flux of the faintest point source detectable in the field of view. Following the same approach as in Hoshino et al. (2010), we estimate the CXB fluctuation by substituting $\Omega_{Bgd} = 0.0069$ deg^2 and $S_c = 1.0 \times 10^{-14}$ erg s^{-1} cm^{-2} from the present XIS observation into the above relation. With this substitution and referring to the values $\sigma_{CXB}/I_{CXB} = 5\%$ and $S_c = 6 \times 10^{-12}$ erg s^{-1} cm^{-2} from the *Ginga* satellite (Hayashida et al. 1989), we obtain $\sigma_{CXB}/I_{CXB} = 13\%$. We thus intentionally change the background intensity by $\pm 13\%$ and find that this does not significantly influence the resulting spectral parameters.

- For (ii), the *Suzaku* XRT has a wide PSF (half power diameter $2'$) that allows photons from adjacent regions to contaminate the data. To avoid significant photon mixing, we set the width of annular regions larger than $2'$ for the outer rings. Simulations by `xissim` raytracing show that, in terms of the fraction of photons, the PSF effect is 40% for $r = 5'-8'$, whereas it is as small as 20% for the outermost ($r = 8'-12'$) ring.

- (iii) In the NE region, many point sources were detected by *XMM-Newton* (Fig. 1), and the contamination of the cluster spectra from their emission may not be negligible, although they were removed with the $r = 1'$ circle. To check their impact, we extracted *XMM-Newton* spectra of the point sources and fitted them to the power-law model. Because of the poor photon statistics (only 260 counts), the photon index was fixed at $\Gamma = 1.5$. The resulting power-law flux was $(1.3 \pm 0.2) \times 10^{-13}$ erg s^{-1} cm^{-2} in the 0.2–12 keV band, which
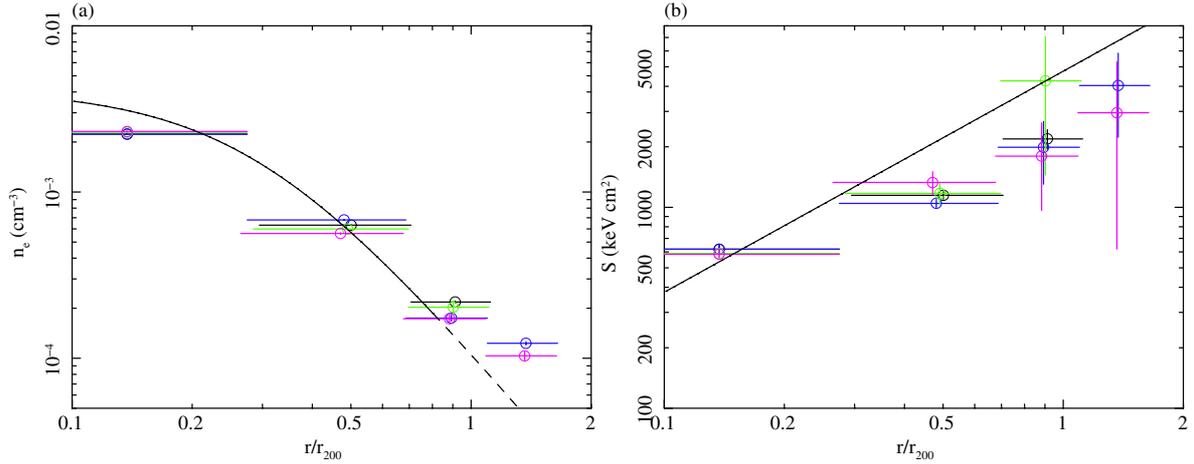
Fig. 5. a) Electron density and **b)** entropy profiles derived from deprojection analysis. The meanings of colors are the same as in Fig. 4. In panel **a)**, the solid line represents the β-model from ROSAT data (Ota & Mitsuda 2004). Since the β-model parameters were derived within $r < 1.6$ Mpc, its extrapolation outside that radius is shown by the dashed line. In panel **b)**, the solid line shows the baseline entropy profile, $S \propto r^{1.1}$ (Voit et al. 2005).

corresponds to 30% of the observed flux in the region of interest. Then, we fitted the XIS spectra of the entire NE $5'-8'$ region to a two-component model consisting of the APEC model and the $\Gamma = 1.5$ power-law model whose normalization was fixed to the best-fit value. The gas temperature was obtained as $kT = 8.2^{+2.3}_{-1.5}$ keV in this case. This is marginally lower than the value in Table 4, $kT = 13.6^{+8.2}_{-4.4}$ keV, but has an overlap within the errors. To accurately estimate the errors, we assigned $\Delta T = 5$ keV (a difference between the two best-fit values) to a systematic error of the temperature in NE $5'-8'$ region. By adding statistical and systematic errors in quadrature, we obtained $kT = 13.6^{+9.6}_{-6.7}$ keV. In Figs. 4−6 and Eq. (3), we show error ranges calculated by considering systematic errors.

3.4. Deprojection analysis

To derive the radial profiles of gas density and entropy, we performed a deprojection analysis of the annular spectra under the assumption that the cluster gas distribution is spherically symmetric. Although we know that A2744 has an irregular X-ray morphology, the deprojection analysis allows the gas properties to be compared with those of other clusters (deduced under the same assumption).

The APEC model corrected for the Galactic absorption was fit to each radial bin with the assumption that the metal abundance is radially constant. The arithmetic deprojection operation was performed by the "projct" model in XSPEC. The two panels in Fig. 5 show the electron density and entropy profiles where the radius is normalized by r_{200}. The electron density was calculated from the APEC normalization factor $\int n_e n_H dV / (4\pi(1 + z)^2 D_A^2)$ [10^{-14} cm^{-5}], where $n_e = 1.2 n_H$. The entropy, defined as $S \equiv kT n_e^{-2/3}$ (Voit 2005), is calculated by substituting the electron density and the temperature derived from the deprojection analysis for each radial bin.

4. Discussion

With *Suzaku*, the profiles of temperature, gas density, and entropy were measured out to $r_{200} \sim 2$ Mpc in A2744. In this section, to discuss the gas heating process in the cluster outskirts
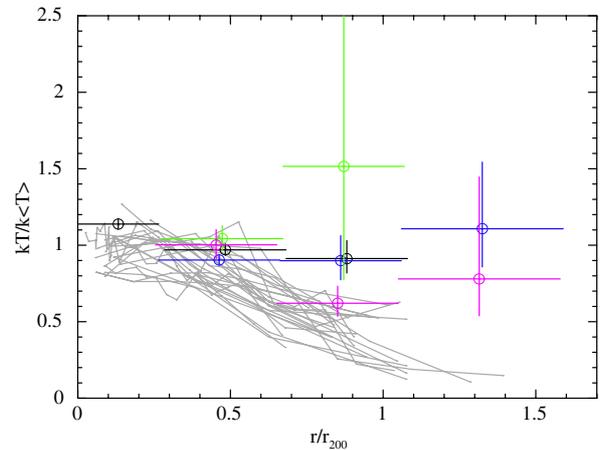

Fig. 6. Comparison of radial temperature profile between A2744 All (black), NW (blue), NE (green), S (magenta), and *Suzaku* sample (gray lines, Reiprich et al. 2013).

and the evolutionary stage of this unique object, the gas properties of A2744 are compared with X-ray observations of other clusters, as well as with multiwavelength data of this cluster.

4.1. Gas properties in cluster outskirts

Figure 6 compares A2744's azimuthally-averaged temperature profile (Sect. 3.2) with currently available *Suzaku* profiles taken from the literature (Reiprich et al. 2013, and references therein). Although the nearby clusters show a systematic temperature decline by a factor of 3 to r_{200}, A2744 has a flat temperature distribution, and the temperature near r_{200} is one of the highest among them. This result indicates that some significant heating process is at work in the cluster outskirts.

In Fig. 5a, the best-fit β-model gas-density profile obtained from the ROSAT/HRI data (Ota & Mitsuda 2004) is shown for comparison. Because the β-model analysis was performed by using the cluster image within $r < 1.6$ Mpc, the density profile is extrapolated outside that radius. Overall, the present result agrees well with that of the β-model within the virial radius for all directions. On the other hand, some flattening is seen in the outermost region. A similar effect was reported for other

Table 5. Gas temperature and galaxy surface density in outer regions of A2744

| Region | $r/r_{200} = 0.69-1.10$ | | $r/r_{200} = 1.10-1.65$ | |
	X-ray temperature kT [keV]	Galaxy surface density Σ [arcmin^{-2}]	X-ray temperature kT [keV]	Galaxy surface density Σ [arcmin^{-2}]
NW	$8.05^{+0.78}_{-0.68}$	0.72 ± 0.14	$9.92^{+2.10}_{-1.56}$	0.50 ± 0.08
NE	$13.58^{+3.74}_{-3.14}$	0.14 ± 0.06	$-^a$	0.29 ± 0.06
S	$5.56^{+0.60}_{-0.50}$	0.82 ± 0.15	$6.99^{+2.70}_{-1.53}$	0.27 ± 0.06
Average	8.15 ± 0.53	0.54 ± 0.07	9.77 ± 1.58	0.35 ± 0.04

Notes. The 1σ statistical errors are quoted. $^{(a)}$ For NE, $r/r_{200} = 1.10-1.65$ is outside the XIS field of view.

clusters, such as A1689 (Kawaharada et al. 2010) and A1795 (Bautz et al. 2009).

Based on simulations considering gravitational heating because of smooth mass accretion, Voit et al. (2005) note that the radial gas entropy profile in clusters tends to follow a power-law, $S(r) \propto T_{200}r^{1.1}$, that can be used as a baseline for assessing the impact of nongravitational processes in the ICM. Figure 5b shows the baseline profile calculated for $kT_{200} = 9.0$ keV. The entropy profiles at $r < r_{200}$ are flatter than predicted by the baseline profile, as observed in other nearby clusters (Walker et al. 2012). At $r \gtrsim r_{200}$, however, the entropy of A2744 shows no clear drop in the outskirts, unlike the previous *Suzaku* results (Walker et al. 2012). This suggests that the thermal properties of ICM in the cluster outskirts should be significantly affected by the complex merging activities in this system, which are examined below by comparing them with multiwavelength observations.

4.2. Comparison between X-ray and optical observations

To examine a relationship between the gas property and galaxy distribution in outer regions of the cluster, we compare the gas temperature with the galaxy surface density. The galaxy density was calculated by using the galaxy catalog in Table 5 of Owers et al. (2011), who compiled two photometric catalogs based on the Supercosmos Sky Survey (Busarello et al. 2002) and the Very Large Telescope (Braglia et al. 2009). We selected 442 galaxies that meet the same criterion as in Boschin et al. (2006): $cz_{cluster} \pm 5000$ km s^{-1} (or $z_{cluster} \pm 0.0167$) and the r_F-band magnitude $r_F < 23$. The following result does not significantly change if we select galaxies with the same criterion as used in A1835 at $z = 0.25$, $r_F < 22$, and $cz_{cluster} \pm 3000$ km s^{-1} (Ichikawa et al. 2013).

Table 5 shows the gas temperature measured by *Suzaku* and the galaxy density for two radial ranges; namely, $0.69 < r/r_{200} < 1.10$ and $1.10 < r/r_{200} < 1.65$. The ranges are normalized by their mean values in each radial bin, and the errors indicate the statistical uncertainties at 68% confidence. In Fig. 7, the temperature deviation $(T - \langle T \rangle)/\langle T \rangle$ is plotted as a function of the galaxy density contrast, $(\Sigma - \langle \Sigma \rangle)/\langle \Sigma \rangle$.

As is clear from Table 5, the galaxy density is anisotropic. For $0.69 < r/r_{200} < 1.10$, we confirm the galaxy excess in the NW and S directions where the filaments have already been identified by Braglia et al. (2007). On the other hand, the galaxy density is significantly lower in the NE direction. For larger radii $(1.10 < r/r_{200} < 1.65)$, however, the density in the NE direction is comparable to the mean. If compared with the gas temperature (Fig. 7), no simple one-to-one correspondence exists between the optical and X-ray properties. These results differ from previous reports on A1689 and A1835 that claimed a positive corre-
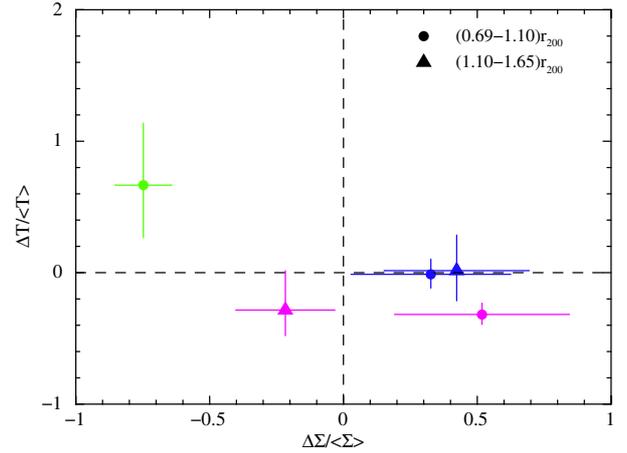

Fig. 7. Comparison of temperature deviation $\Delta T/\langle T \rangle$ and galaxy surface density contrast $\Delta\Sigma/\langle\Sigma\rangle$ in the outskirts of A2744. The data for the two radial bins $(0.7-1.1)r_{200}$ and $(1.1-1.6)r_{200}$ are shown by circles and triangles, respectively. The meanings of colors are the same as in Fig. 4. The quoted errors are the 1σ statistical uncertainties.

lation between galaxy density and gas temperature (Kawaharada et al. 2010; Ichikawa et al. 2013). Therefore, the present result strongly suggests a complex dynamical state and mass structure in A2744.

4.3. Comparison between X-ray and radio observations

From the *Suzaku* observation, we found a hint of a temperature jump in the NE region. In fact, as seen from Fig. 8, the location of the high-temperature region coincides well with that of the large radio relic. Thus, the gas may have undergone shock heating because of merging or mass accretion onto the main cluster. For A3667, a sharp change in both temperature and brightness near the relic was observed (Finoguenov et al. 2010; Akamatsu et al. 2012a). With the current photon statistics of the *Suzaku* data in the NE region, however, we find no significant discontinuity in the X-ray surface brightness at the radio relic. To clarify the origin of the high-temperature gas in the NE region and its relationship to the radio relic, we will examine the temperature and density structures in more detail upon completion of an additional pointing observation approved for *Suzaku* AO8.

4.4. X-ray mass estimation and implications

The complex gas distribution in A2744 indicates that the cluster is not in the relaxed state. However, we expect that comparing the hydrostatic mass estimated from X-ray observations with the gravitational lensing mass will clarify the dynamical
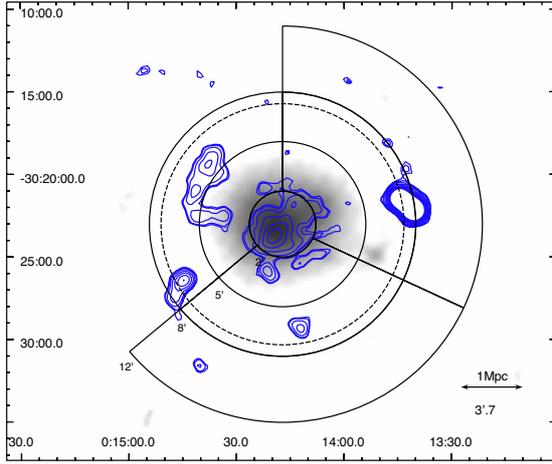
Fig. 8. *Suzaku*-XIS image (gray scale) overlaid with radio 325 MHz intensity contours (blue) (Orrú et al. 2007). A radio halo and radio relic extending over 1 Mpc in length exist at the cluster core and at 7′ (or $0.8r_{200}$) NE of the center, respectively. The XIS spectral regions (black) and virial radius (r_{200} = 7′.3) are also indicated.

state of the system (e.g., Ota et al. 1998). Merten et al. (2011) estimate the weak lensing mass of this cluster to be $M_{\mathrm{lens}}(r < 1.3\,\mathrm{Mpc}) = (1.8 \pm 0.4) \times 10^{15}\,M_\odot$. From the radially-averaged temperature profile (All: $0-360°$) derived in Sect. 3.4 and the β-model parameters $\beta = 0.96$ and $r_{\mathrm{c}} = 133$ kpc (Ota & Mitsuda 2004), we calculate the hydrostatic mass projected within a radius of 1.3 Mpc to be

$$M_{\mathrm{X}}(<1.3\,\mathrm{Mpc}) = 1.7^{+0.2}_{-0.2} \times 10^{15}\,M_\odot. \tag{1}$$

If the temperature profiles in three different directions are separately used, we obtain

$$M_{\mathrm{X}}(<1.3\,\mathrm{Mpc}) = 1.4^{+0.5}_{-0.4} \times 10^{15}\,M_\odot \quad \text{for NW}, \tag{2}$$

$$M_{\mathrm{X}}(<1.3\,\mathrm{Mpc}) = 2.9^{+2.6}_{-1.9} \times 10^{15}\,M_\odot \quad \text{for NE}, \tag{3}$$

$$M_{\mathrm{X}}(<1.3\,\mathrm{Mpc}) = 1.3^{+0.7}_{-0.4} \times 10^{15}\,M_\odot \quad \text{for S}. \tag{4}$$

Excluding the NE region where the high-temperature gas exists, the systematic uncertainty in the X-ray hydrostatic mass is estimated to be 25%. Although the X-ray mass derived from the mean temperature profile agrees with the weak lensing mass within the statistical error, it must be interpreted with care given the systematic uncertainty.

Based on X-ray observations (e.g., Akamatsu et al. 2012a,b) and hydrodynamic simulations (e.g., Akahori & Yoshikawa 2010), a possibility of non-equilibrium ionization in merging clusters has been pointed out. Assuming that the ionization timescale is given by $n_{\mathrm{e}}t = 10^{12}$ cm^{-3} s (Masai 1984) and the observed high-temperature gas originates in the merger shock having a shock velocity on the order of 2000 km s^{-1}, the ion-electron relaxation timescale near the virial radius of A2744 is likely to be longer than the time elapsed after the shock occurs. A more quantitative evaluation of the physical state of the ICM requires an additional observation.

5. Summary

By using the *Suzaku* XIS detectors, we performed an X-ray spectral analysis of the merging cluster A2744 at $z = 0.3$ and derived the temperature profiles out to large radii (r_{200} in the NE direction and $1.5r_{200}$ in the NW and S directions) for the first time.

The temperature is as high as $kT \sim 9$ keV even near the virial radius and does not decline significantly in the outskirts, which differs from all other clusters observed with *Suzaku*. We also found that the temperature structure is anisotropic and exhibits no clear positive correlation with the galaxy surface density, suggesting that the cluster has a very complex mass structure and is dynamically young. We find a hint of temperature jump in the NE region, and its location coincides with that of a large radio relic. Thus the gas may have undergone shock heating because of merging or mass accretion. A further examination of the shock structure near the radio relic must await a follow-up X-ray observation of the NE region.

References

Akahori, T., & Yoshikawa, K. 2010, PASJ, 62, 335
Akamatsu, H., de Plaa, J., Kaastra, J., et al. 2012a, PASJ, 64, 49
Akamatsu, H., Takizawa, M., Nakazawa, K., et al. 2012b, PASJ, 64, 67
Anders, E., & Grevesse, N. 1989, Geochim. Cosmochim. Acta, 53, 197
Arnaud, M., Pointecouteau, E., & Pratt, G. W. 2005, A&A, 441, 893
Bautz, M. W., Miller, E. D., Sanders, J. S., et al. 2009, PASJ, 61, 1117
Boschin, W., Girardi, M., Spolaor, M., & Barrena, R. 2006, A&A, 449, 461
Braglia, F., Pierini, D., & Böhringer, H. 2007, A&A, 470, 425
Braglia, F. G., Pierini, D., Biviano, A., & Böhringer, H. 2009, A&A, 500, 947
Busarello, G., Merluzzi, P., La Barbera, F., Massarotti, M., & Capaccioli, M. 2002, A&A, 389, 787
Finoguenov, A., Böhringer, H., & Zhang, Y.-Y. 2005, A&A, 442, 827
Finoguenov, A., Sarazin, C. L., Nakazawa, K., Wik, D. R., & Clarke, T. E. 2010, ApJ, 715, 1143
Govoni, F., Enßlin, T. A., Feretti, L., & Giovannini, G. 2001a, A&A, 369, 441
Govoni, F., Feretti, L., Giovannini, G., et al. 2001b, A&A, 376, 803
Hayashida, K., Inoue, H., Koyama, K., Awaki, H., & Takano, S. 1989, PASJ, 41, 373
Hoshino, A., Henry, J. P., Sato, K., et al. 2010, PASJ, 62, 371
Ichikawa, K., Matsushita, K., Okabe, N., et al. 2013, ApJ, 766, 90
Ishisaki, Y., Maeda, Y., Fujimoto, R., et al. 2007, PASJ, 59, 113
Kalberla, P. M. W., Burton, W. B., Hartmann, D., et al. 2005, A&A, 440, 775
Kawaharada, M., Okabe, N., Umetsu, K., et al. 2010, ApJ, 714, 423
Kempner, J. C., & David, L. P. 2004, MNRAS, 349, 385
Koyama, K., Tsunemi, H., Dotani, T., et al. 2007, PASJ, 59, 23
Kushino, A., Ishisaki, Y., Morita, U., et al. 2002, PASJ, 54, 327
Masai, K. 1984, Ap&SS, 98, 367
Merten, J., Coe, D., Dupke, R., et al. 2011, MNRAS, 417, 333
Mitsuda, K., Bautz, M., Inoue, H., et al. 2007, PASJ, 59, 1
Orrú, E., Murgia, M., Feretti, L., et al. 2007, A&A, 467, 943
Ota, N., & Mitsuda, K. 2004, A&A, 428, 757
Ota, N., Mitsuda, K., & Fukazawa, Y. 1998, ApJ, 495, 170
Ota, N., Fujino, Y., Ibaraki, Y., Böhringer, H., & Chon, G. 2013, A&A, 556, A21
Owers, M. S., Randall, S. W., Nulsen, P. E. J., et al. 2011, ApJ, 728, 27
Pierini, D., Zibetti, S., Braglia, F., et al. 2008, A&A, 483, 727
Reiprich, T. H., Basu, K., Ettori, S., et al. 2013, Space Sci. Rev., 177, 195
Sakuma, E., Ota, N., Sato, K., Sato, T., & Matsushita, K. 2011, PASJ, 63, 979
Serlemitsos, P. J., Soong, Y., Chan, K.-W., et al. 2007, PASJ, 59, 9
Smith, R. K., Brickhouse, N. S., Liedahl, D. A., & Raymond, J. C. 2001, ApJ, 556, L91
Snowden, S. L., Egger, R., Freyberg, M. J., et al. 1997, ApJ, 485, 125
Tawa, N., Hayashida, K., Nagai, M., et al. 2008, PASJ, 60, 11
Uchiyama, Y., Maeda, Y., Ebara, M., et al. 2008, PASJ, 60, 35
Voit, G. M. 2005, Rev. Mod. Phys., 77, 207
Voit, G. M., Kay, S. T., & Bryan, G. L. 2005, MNRAS, 364, 909
Walker, S. A., Fabian, A. C., Sanders, J. S., & George, M. R. 2012, MNRAS, 427, L45
Zhang, Y.-Y., Finoguenov, A., Böhringer, H., et al. 2004, A&A, 413, 49
Zhang, Y.-Y., Böhringer, H., Finoguenov, A., et al. 2006, A&A, 456, 55